Biophysical *Journal*
Computational Tool

Biophysical Society

Quantifying Intracellular Particle Flows by DIC Object Tracking

Anushree R. Chaphalkar,[1] Yash K. Jawale,[1] Dhruv Khatri,[1] and Chaitanya A. Athale[1,*]
[1]Division of Biology, Indian Institute of Science Education and Research, Pune, Pashan, Pune, Maharashtra, India

ABSTRACT Label-free imaging techniques such as differential interference contrast (DIC) allow the observation of cells and large subcellular structures in their native, unperturbed states with minimal exposure to light. The development of robust computational image-analysis routines is vital to quantitative label-free imaging. The reliability of quantitative analysis of time-series microscopy data based on single-particle tracking relies on accurately detecting objects as distinct from the background, i.e., segmentation. Typical approaches to segmenting DIC images either involve converting images to those resembling phase contrast, mimicking the optics of DIC object formation, or using the morphological properties of objects. Here, we describe MATLAB based, single-particle tracking tool with a GUI for mobility analysis of objects from in vitro and in vivo DIC time-series microscopy. The tool integrates contrast enhancement with multiple modified Gaussian filters, automated threshold detection for segmentation and minimal distance-based two-dimensional single-particle tracking. We compare the relative performance of multiple filters and demonstrate the utility of the tool for DIC object tracking (DICOT). We quantify subcellular dynamics of a time series of *Caenorhabditis elegans* embryos in the one-celled stage by detecting birefringent yolk granules in the cytoplasm with high precision. The resulting two-dimensional map of oscillatory dynamics of granules quantifies the cytoplasmic flows driven by anaphasic spindle oscillations. The frequency of oscillations across the anterior-posterior (A-P) and transverse axes of the embryo correspond well with the reported frequency of spindle oscillations. We validate the quantitative accuracy of our method by tracking the in vitro diffusive mobility of micron-sized beads in glycerol solutions. Estimates of the diffusion coefficients of the granules are used to measure the viscosity of a dilution series of glycerol. Thus, our computational method is likely to be useful for both intracellular mobility and in vitro microrheology.

SIGNIFICANCE Differential interference contrast (DIC) time-lapse microscopy is widely used in cell and developmental biology as a label-free method involving minimal perturbation. Single-particle tracking tools specific to DIC microscopy are lacking. We have developed a computational tool for DIC object detection and tracking with a GUI and demonstrate its utility by tracking intracellular yolk granules in the crowded cytoplasm of one-celled *Caenorhabditis elegans* embryos. The frequency of the oscillatory flows of the granules compares well with that of spindle oscillation. Our method is also validated by tracking the Brownian motion of micron-sized beads to estimate the viscosity of solutions in vitro. This tool could have wider relevance for biophysical measurements of cellular mobility and subcellular mechanics.

INTRODUCTION

Label-free microscopy is widely used to study transparent cells and tissues. In particular, differential interference contrast (DIC) or Nomarski (1) and phase-contrast microscopy (2) are standard modes built into biological microscopes to generate image contrast using inherent features such as the anisotropy of refractive index and density. Although fluorescence microscopy offers the advantage of molecular specificity, the phototoxicity resulting from such an approach in live imaging can alter cell physiology (3). Because of the inherent advantages of reduced light exposure and minimal intervention in the sample, label-free in vivo microscopy combined with computational image analysis continues to be relevant. Image segmentation of phase-contrast images is relatively simpler because it involves distinguishing dark objects against a bright background. As a result, a wide variety of computational methods have been successfully developed to quantify cellular and subcellular objects in phase-contrast images (4–7). Objects in DIC images, on the

Submitted April 22, 2020, and accepted for publication December 10, 2020.
*Correspondence: cathale@iiserpune.ac.in
Anushree R. Chaphalkar and Yash K. Jawale contributed equally to this work.
Editor: Jason Swedlow.
https://doi.org/10.1016/j.bpj.2020.12.013

other hand, are represented as a combination of light and dark regions, giving a pseudo-three-dimensional effect, with a typically gray background. Segmentation of such images is more involved, with previous approaches relying on either converting them to "pseudophase" (8) or extracting low-level information such as gradient (9,10), shear direction (11,12), spatial filtering using "Mexican hat" kernels to denoise combined with region-max to segment (13), and brightness fluctuations (14). Although shape-specific methods have been successfully used for tracking the dynamics of filopodia (15) and microtubules (MTs) (14,16), they are limited in their utility. Some alternative methods to particle tracking include particle image velocimetry, which for example, has been used to quantify intracellular flows by occurring after yolk-granule mobility in DIC images (17), optical flow methods (18), and differential dynamic microscopy based on intensity fluctuation statistics in images (19) that have been used to measure ciliary beat frequencies in vivo (20). Although such methods are robust and work on in vivo data, ignoring the individual identity of objects potentially could result in missing out in changes in as a function of position or time. This in turn could lead to ignoring important local effects that might be functionally related to in vivo heterogeneity in mobility. The absence of a robust and general solution to detect intracellular structures in DIC at high particle densities has hindered further quantification of label-free images.

Caenorhabditis elegans embryos are ideal samples for in vivo computational imaging in DIC because they are optically transparent and lack pigments. DIC-microscopy-based mutational screens have been used to understand embryonic cell divisions (21) and spindle mechanics (22). Algorithms used to identify features in *C. elegans* embryos include a shortest path method to automatically identify embryo stages and quantify boundary dynamics during divisions (23,24). Similarly, active contours have been used to track spindle dynamics (25,26). The analysis of intracellular dynamics by segmentation-based approaches has been restricted to quantifying centrosome positional dynamics (22,27,28). At the same time, detailed theoretical models of the mechanics anaphase spindles and their oscillations in *C. elegans* based on molecular motors and MTs have been developed (29–31). However, a comparison between theoretical predictions and experiments continues to be limited by the methods available for noninvasive measurement of intracellular mechanics. Although label-free quantitative microscopy could address this need, it requires the development of methods for precise segmentation in a crowded environment from such images.

Here, we describe a DIC-object-tracking (DICOT) method that combines a novel filtering approach that we refer to as scaling of Gaussian (SoG). Combined with a distance-based, single-particle tracking approach, we employ it to analyze in vivo cytoplasmic flow dynamics in a one-cell *C. elegans* embryo and as a means of estimating viscosity from bead diffusion in glycerol solutions.

MATERIALS AND METHODS

DIC segmentation and tracking

We implement multiple filters combined with automated threshold detection to segment objects in each frame, followed by a minimal distance tracking method to connect object and build tracks. As a first step, the user chooses one of the filters: Gaussian, difference of Gaussian (DoG), inverse Laplacian of Gaussian (iLoG), or an SoG. The SoG filter is calculated as a difference between a Gaussian function h_G with a filter of size k_{size} and a standard deviation σ and the following scaled mean:

$$h_{SoG} = h_G - \langle h_G \rangle (\lambda - \phi), \tag{1}$$

where ϕ is the strength of the difference-based scaling by the mean and λ is a switch parameter typically set to 1 for DIC images. A value of $\lambda = -1$ is useful for dark objects against a bright background. The steps involved in the process of filtering and segmentation are described in the Algorithm Box (Supporting Materials and Methods) and Fig. 1. The filter is a modified Gaussian and comparable with a DoG filter because of the subtraction operation. Of the four user-provided inputs to SoG, two are easily determined by the user with $\lambda = 1$ for DIC images and the kernel size k_{size} estimated from the characteristic size of the objects, with the only free parameters being the standard deviation σ of the Gaussian and sensitivity (S) factor ϕ for scaling by the mean, which control the spread and height of the filter, respectively. The filter is implemented in MATLAB (The MathWorks, Natick, MA).

The filtered image is contrast adjusted by scaling between the minimal and maximal values of the histogram and segmented by using the p^{th} root of the value output by Otsu's method, τ. We find $\sqrt{\tau}$, i.e., p = 2, to be optimal for the objects we have tested.

Segmentation results in centroids of multiple granule (Fig. 1 *b*) that are connected to form tracks based on two input parameters: 1) search radius (r_s) to define the local neighborhood that depends on particle velocity, and 2) minimal time frames (T_{min}), which a track spans. The pair-wise distance $d_j(\Delta t)$ between every j^{th} centroid in successive frames t and $t + \Delta t$ are linked if the minimal distance is less than the search radius r_s. Centroids that do not form a part of any trajectory are treated as new start points. To avoid artifacts due to poor statistics, short tracks are eliminated if they span less than T_{min} number of frames. Image noise was simulated as multiplicative speckle noise with zero mean and increasing variance using the inbuilt function imnoise in MATLAB (The MathWorks), and the error of positional accuracy was tested by finding the distance between the ground truth (GT) and the automated detection in a representative frame from a DIC image time series of the *C. elegans* embryo.

Embryo time series

Multiple time series of *C. elegans* N2 embryos (N2_15, N2_18, and N2_20) were taken from a published database (http://www.ens-lyon.fr/LBMC/NematodeCell/2010/12/) reported by Valfort et al. (32). Typically 450 frames ($\Delta t = 0.5$ s) were analyzed by selecting a subset of frames corresponding to the onset of anaphase spindle oscillations.

Microscopy of bead suspensions in glycerol

Glycerol (99% GC; Sigma-Aldrich) solutions in water with increasing concentrations 0, 10, 20, 30 and 40% (vol/vol) were used to resuspend monodisperse polystyrene beads (National Institute of Standards and Technology Traceable Particle Size Standards; Bangs Laboratories, Fishers, IN) of a diameter of 1 μm. For diffusion measurements, the beads were diluted 1:100 (vol/vol) to get sufficient separation, so their mobility can be considered to be independent of crowding effects. The solution containing the bead suspension was flowed into a double-backed tape chamber (dimensions: 1 cm × 1 cm × 0.01 cm) sandwiched between a

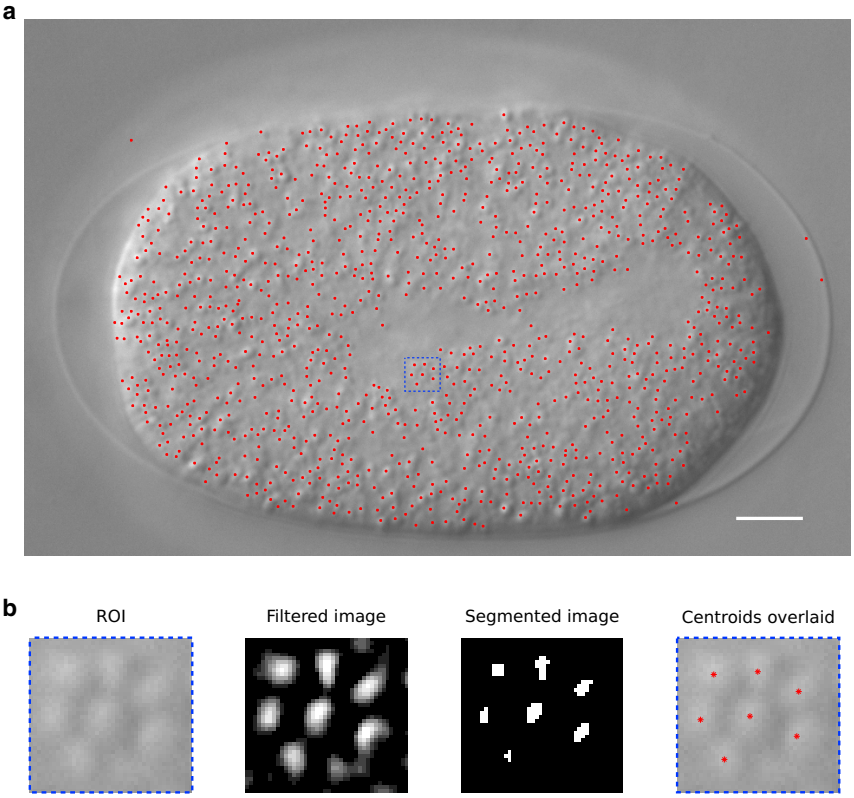

FIGURE 1 Detecting yolk-granules in a *C. elegans* embryo in DIC. (*a*) The yolk granules of a *C. elegans* embryo in the one-celled stage in DIC microscopy from the mid-plane are segmented using a novel scaling of Gaussian (SoG) method combined with automated thresholding. Scale bar, 5 μm. (*b*) The workflow is described using a representative region of interest (ROI) of the embryo image (*box with dashed blue line* from (*a*)); shown is a filtered image by convolving the image with an SoG filter (parameters: $k_{size} = 9$ and $\sigma = 1.25$), resulting in enhanced contrast; shown is a segmented image obtained by thresholding by a modified Otsu's method; and centroids of detected objects (*asterisk*) are overlaid on the original image. To see this figure in color, go online.

slide and a coverslip (Medicos Supplies, Pune, India). Samples were imaged using a 40× (NA 0.9 or 0.65 ELWD) lens on a Nikon Eclipse Ti-E inverted microscope (Nikon, Tokyo, Japan) at 30°C by a temperature control system (Okolab, Pozzuoli, Italy). Images were acquired every 0.5 s for 1 min with an Andor Clara2 CCD camera (Andor Technology, Belfast, UK).

Data analysis

The yolk granules were classified into four regions based on the apparent axis along which they were maximally displaced: anterior (A), posterior (P), or one of the transverse axes—transverse 1 (T1) or transverse 2 (T2). The *x*- and *y*-positions with time were used to calculate the distance from their respective origins in *x* (Δx) and *y* (Δy), and the distance was averaged for each region (Δy for the A-P axis and Δx for the T1-T2 axis). The frequency of oscillation was estimated using a fast Fourier transform. An average curve was estimated for each region as follows:

1) Shift the origin of the position time series of the yolk granules, $r_{j,t}$ (where *r* is either the *x*- or *y*-position), with respect to their initial positions in x (Δx) and y (Δy), resulting in a new series $r^*_{j,t}$:

$$i = 0 \begin{cases} r^*_{j,t} = & r_{j,t} - r_{j,1} \\ \overline{r}_{(i=0)} = & \dfrac{\sum_{j\,|\,t} r^*_{j,t}}{n_{j\,|\,t}} \end{cases}, \tag{2}$$

where *n* is the number of tracks at a given time point *t* and *j* represents the identity of the track.

2) Calculate the average time-series $\overline{r}_i$ for the i^{th} iteration by estimating the deviation of every particle from the average curve obtained at the previous iteration $(i-1)$, subtracting the mean deviation ($\langle \Delta r_{j,t} \rangle$) and averaging over each track at a given time point ($n_{j|t}$) for all time points as follows:

$$i > 0 \begin{cases} \Delta r_{j,t} = & r_{j,t} - \overline{r}_{i-1} \\ r^*_{j,t} = & r_{j,t} - \langle \Delta r_{j,t} \rangle \\ \overline{r}_i = & \dfrac{\sum_{j\,|\,t} r^*_{j,t}}{n_{j\,|\,t}} \end{cases}. \tag{3}$$

3) Consider the curve to be the optimal average curve and stop the iteration when the global deviation across all tracks *N* is smaller than a threshold value δ:

$$i{+}{+}, \text{iff} \left\{ \frac{\sum_j^N \langle \Delta r_{j,t} \rangle}{N} \geq \delta. \right. \tag{4}$$

We find the global deviation saturates for $\delta < 10^{-4}$ within 5–10 iterations. All data analysis was performed using a code written in MATLAB R2017b (The MathWorks).

Estimating the diffusion coefficient of bead mobility

The effective diffusion coefficient (D) of bead motility was estimated from a fit to the mean-square displacement (MSD) plot as a function of time

interval (t) using methods described previously (33,34). The anomalous diffusion model $MSD = 4 \times D_{eff} \times t^{\alpha}$ was applied to the MSD data using a Levenberg-Marquardt nonlinear least-square routine implemented in both MATLAB (The MathWorks) and SciPy (Python 3.6) (35). The anomaly parameter α was found to be ~1, indicating diffusion without drift or restriction.

As an alternative method to cross-check our estimates, we measured the diffusion coefficient of beads based on an approach originally described by Perrin (36). The displacement along the x (Δx) and y axes (Δy) for every successive step of each trajectory were plotted in a frequency histogram and fit to a standard Gaussian expression:

$$P(\Delta x) = \frac{1}{\sigma\sqrt{2\pi t}} \exp^{-\Delta x^2/2\sigma^2}, \tag{5}$$

where σ is the standard deviation for one-dimensional diffusion that is related to the diffusion coefficient (D) by $\sigma = \sqrt{2Dt}$.

The viscosity η was estimated from Stokes-Einstein relation $D = k_B T/6\pi\eta r$, where the radius of the beads (r) is 0.5 μm and $k_B T$ is the product of Boltzmann's constant and temperature (K), taken as 4.1 pN-nm.

Code performance and availability

A typical time series with 450 frames of 450 × 300 pixels required 5–10 min to process with 200 particles per frame on a Linux Workstation with two Intel Xeon processors (2.20 GHz) and 64-GB RAM. The program has a GUI-based, user-friendly interface (Fig. S1) compatible with MATLAB2019b and higher (The MathWorks). The source code has been made OpenSource and can be accessed here: https://github.com/CyCelsLab/DICOT. Additionally, we have also released a command-line tool with the source code here https://github.com/CyCelsLab/DICOT_cmd, compatible with MATLAB2017b and higher (The MathWorks), to allow for rapid modifications of the program and the easy addition of new filters.

RESULTS AND DISCUSSION

Testing the detection accuracy of intracellular granules in DIC images

The quality of single-particle tracking (SPT) depends on the accuracy of the object detection. To achieve high-accuracy tracking, we test multiple filtering approaches, Gaussian, inverse Laplacian of Gaussian (iLoG), difference of Gaussian (DoG), and the scaling of Gaussian (SoG). These filters are then combined with segmentation by thresholding based on Otsu's method to detect objects in DIC images. The SoG filter scales a standard Gaussian filter (h_G) with the mean ($\langle h_G \rangle$) and an S factor ϕ as follows:

$$h_{SoG} = h_G - \langle h_G \rangle (\lambda - \phi). \tag{6}$$

When the image contains bright objects against a dark background, typical for both DIC and fluorescence, image λ is set to 1, whereas it is set to -1 for dark objects against a bright background (Fig. S3). The S factor ϕ is used to enhance the degree of contrast between the fore- and background. The SoG filter is a simpler version of the DoG filter $h_{DoG} = h_{G1}(\sigma_1) - h_{G2}(\sigma_2)$, where h_{G1} and h_{G2} are two Gaussians, and σ_1 and σ_2 define the respective spread. For a DoG filter when $\sigma_2 \gg \sigma_1$, the difference approximates SoG (Fig. S2). At the same time, the LoG filter, based on the second derivative of a Gaussian, can also be mapped to DoG under specific conditions of Gaussian filters (37) due in part to the fact that they are based on a Gaussian. However, the simplicity in using SoG scaling on a Gaussian by a scalar value by the use of a single S parameter ϕ and estimation of filter size from object size, as compared with multiple or derivatives of Gaussians, suggests a simplicity that could be more user-friendly for optimization in the analysis of diverse experimental data sets. The filtered images are thresholded based on a modified Otsu's method (38), resulting in object detection.

The detection method appears to identify the majority of birefringent yolk granules in a DIC image time series of *C. elegans* embryos as identifiable by eye (Fig. 1 *a*). The enhanced contrast achieved by SoG filtering allows object segmentation by automated thresholding (Fig. 1 *b*). To quantify the extent of correctly detected yolk granules, we have used six randomly selected frames in the time series in two representative regions of interest (ROIs), one anterior and one posterior, to account for any spatial differences (Fig. 2 *a*; Fig. S4) and marked yolk granules manually to serve as the GT of detection (Fig. 2 *b*). The output from DICOT analysis was then classified based on the Euclidean distance of the granule coordinates (x-y-positions) detected by the algorithm to the "true coordinate" into the following classes.

True positives (TP)

The distance of the centroid identified by the algorithm lies within a threshold (τ_{dist}) distance of the interactively annotated point. A τ_{dist} of two pixels was chosen to account for human error while selecting centroid of granule.

False positives (FP)

Detections obtained from the algorithm at a distance to the GT greater than τ_{dist} are classified as false positives.

False negatives (FN)

All manual annotations that were not detected by the algorithm are classified as false negatives.

To quantify how well DICOT works at object detection, we estimate three variables: sensitivity (S), precision (P), and the F1 score. S is defined as the ratio of correct detections by the algorithm (TP) and all detections both true and false, as described by the following expression:

$$S = \frac{TP}{TP + FN}. \tag{7}$$

An alternative measure, P is the fraction of correctly classified detections out of total detections from the algorithm as given by the following:

$$P = \frac{TP}{TP + FP}. \tag{8}$$

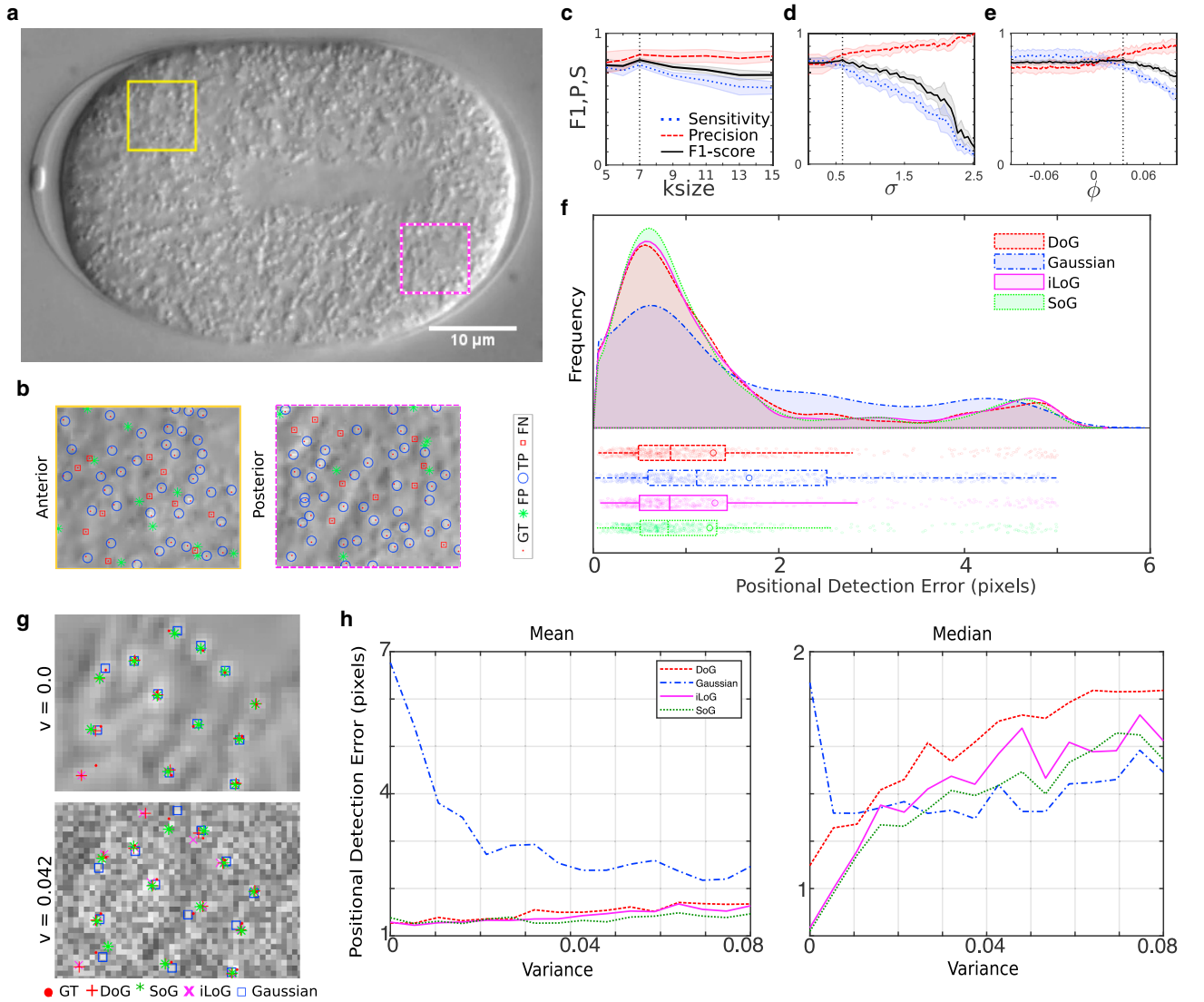

FIGURE 2 P of yolk-granule detection in DIC. (*a*) ROIs from the anterior (A) (*line*) and posterior (*dashed line*) regions of a DIC image time series of a *C. elegans* embryo were used to estimate (*b*) the ground truth (GT; *solid circle*) through manual annotation of granules and classify detections based on the algorithm as either true positives (*open circle*), detected by the algorithm, as well as manually false positives (*asterisk*), those identified by the algorithm but not manually, and false negatives (*open square*), those that were identified manually but the algorithm failed to detect. (*c–e*) The mean ± standard deviation (SD) from n = 6 ROIs measuring S (*dotted line*, Eq. 7), P (*dashed line*, Eq. 8), and the F1 score (*solid line*, Eq. 9) of detection are plotted to examine the effect of three different parameters input to DICOT, namely (*c*) the filter size k_{size} (with σ =0.5949, $\phi = -0.0354$), (*d*) the standard deviation of the filter σ ($k_{size} = 7$), $\phi = 0.0354$), and (*e*) the S factor ϕ (with $\sigma = 0.5949$, $k_{size} = 7$). The fixed values were taken from a systematic scan of all three parameters (Fig. S6) and are marked with a vertical dotted line. (*f*) Shown is the frequency distribution of the positional detection error in pixels based on filtering by either Gaussian (*dash-and-dot line*), inverted iLoG (*solid line*), DoG (*dashed line*), or SoG (*dotted line*) is plotted with (*bottom*) the box-plot representing the data scatter. Here, the following symbols have the described meaning: open circle, mean; midline, median; and whiskers, minimum and maximum. (*g*) The effect of multiplicative speckle noise on positional detection error was examined for a range of variance values of the noise function. Two representative images of variance 0 and 0.042 were filtered based on the optimal parameters for detection by filtering and segmentation based on either Gaussian (*open circle*), iLog (*cross*), DoG (*plus sign*), or SoG (*asterisk*) filters. The error is the distance from the GT (*solid circle*). (*h*) The mean (*left*) and median (*right*) positional detection error for increasing variance of noise ranging is plotted. To see this figure in color, go online.

Finally, the F1-score (F1) combines both measures of P and S as follows:

$$F1 = \frac{2 \times P \times S}{P + S}. \tag{9}$$

We find the S, P, and F1 are affected similarly by kernel size k_{size} and σ (Fig. 2, *c* and *d*), whereas $\phi < 0$ is optimal for S and F1 but not P (Fig. 2 *e*). Increasing the filter size (k_{size}) results in reduced S, whereas P was maximal for values greater than six pixels, and the F1 score is optimal for k_{size}

between five and seven pixels. Based on a comparison between manual detection (Fig. S5 *a*) with SoG, Gaussian, inverted LoG- and DoG-based image filters (Fig. S5, *b–d*) of qualitatively SoG are comparable with LoG and DoG filtering (Fig. S5 *e*). Evaluation of the P, S, and F1 score, compared for two different methods of scoring, suggests that the SoG and DoG are comparable in their performances (Fig. S6, *a–c*). In contrast, we find the statistics of positional detection error is the lowest for SoG compared with the other filtering methods tested in terms of mean, median, and outliers (Fig. 2 *f*). To avoid any biases, we scanned multiple parameters for each filter systematically across a range of comparable values and used those parameters that maximized the F1 score (Fig. S7, *a–d*). Although the error resulting from filtering by SoG, iLoG, and DoG is comparable, we find increasing "noise" in the image (Fig. S8) changes the positional detection error with SoG and iLoG, showing the smallest error and greater robustness compared with the other filters (Fig. 2, *g* and *h*). This suggests that our method is optimal for the analysis of in vivo time series of *C. elegans* embryos. We proceeded to track the granule mobility and quantify the flow in the cytoplasm.

Oscillatory dynamics of yolk granules at anaphase

One-celled embryos of *C. elegans* in the anaphase experience cytoplasmic flows in the midplane driven by MT-motor interactions observed in terms of yolk-granule movement (31,39). This is driven by the oscillatory nature of the

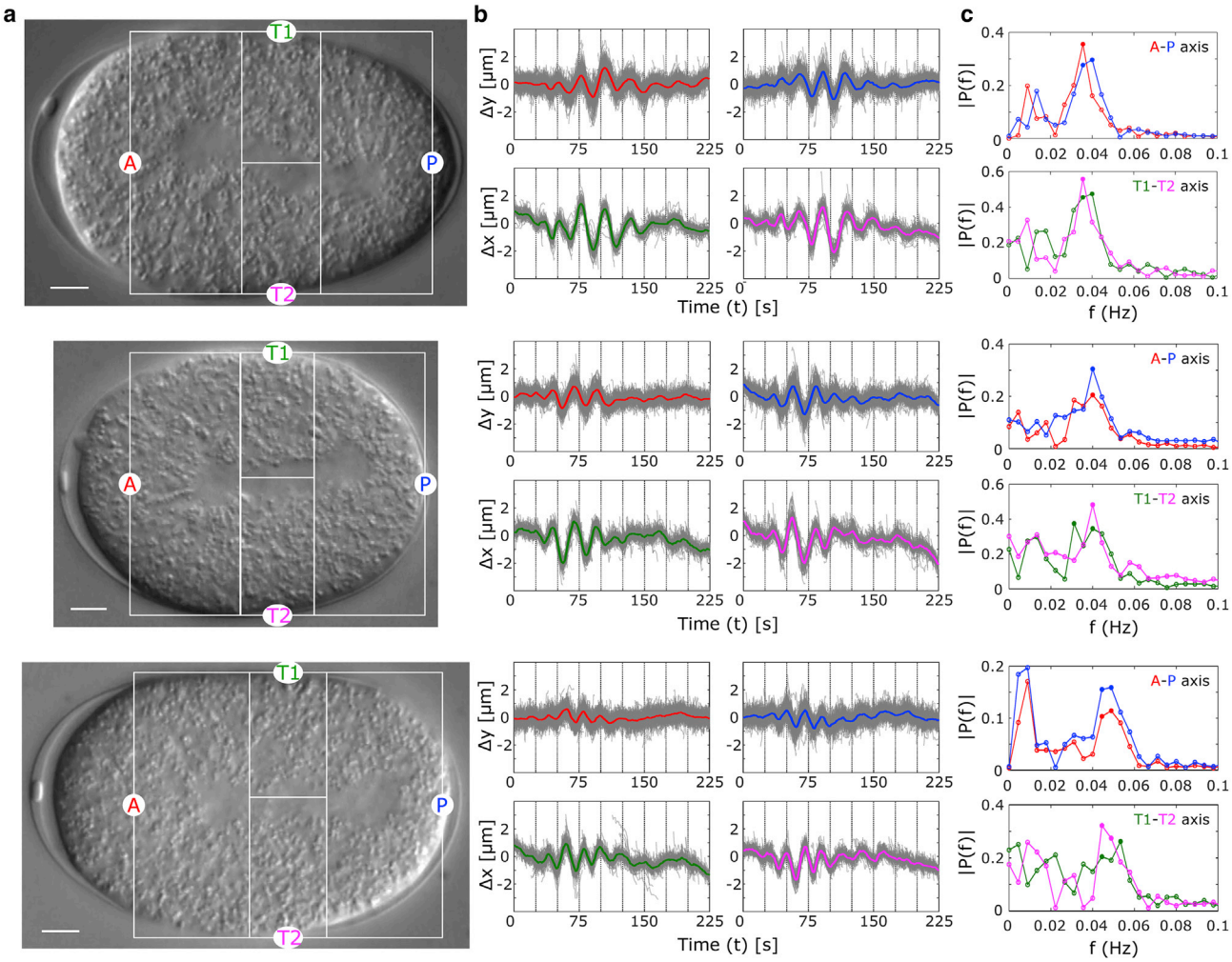

FIGURE 3 In vivo microrheology of *C. elegans* yolk-granule mobility. (*a*) Three representative DIC image time series of the midplane of a *C. elegans* embryo taken from the Valfort et al. data set (32) (N2 embryo time-series N2_15, N2_18, and N2_20 taken from http://www.ens-lyon.fr/LBMC/NematodeCell/2010/12/) are marked to highlight the regions of the embryo in which yolk-granule mobility was analyzed: the anterior (A; *red*), posterior (P; *blue*), and two transverse regions, T1 (*green*) and T2 (*magenta*). Scale bar, 5 μm. (*b*) The change in position along x (Δx) across the transverse axes and in y (Δy) across the A-P axes of individual granules are plotted as a function of time (*gray lines*). Colored lines represent the mean profiles for the A (*red*), P (*blue*), T1 (*green*), and T2 (*magenta*) regions. (*c*) The probability of oscillatory frequencies, P(f), is plotted from mean distance-time data for A (*red*), P (*blue*), T1 (*green*), and T2 (*magenta*) regions (*open circle*). Solid circles indicate the dominant frequencies. For color references, please refer to the online edition. To see this figure in color, go online.

spindle movement, which has been quantified in previous work (25,26,31,32). Because yolk granules are thought to be passively mobile in the cytoplasm (22), our approach to particle tracking could provide a spatial map of this cytoplasmic mobility driven by spindle oscillations. We can successfully track multiple DIC image time series of the midplane of these embryos and classify them into anterior (A), posterior (P), or two transverse regions, T1 and T2 (Fig. 3 *a*; Video S1), because granules remain largely relatively restricted to a region of the embryo. The time-dependent displacement of granules along either the *y* axis for regions A and P, or along the *x* axis for T1 and T2, display oscillatory behavior that is captured by an average curve (Fig. 3 *b*) obtained by iterative optimization to individual trajectories (Fig. S9). The oscillations along the two axes A-P and T1-T2 are out of phase, as expected from spindle geometry and the incompressible nature of the cytoplasm. The dominant frequency of oscillation based on Fourier

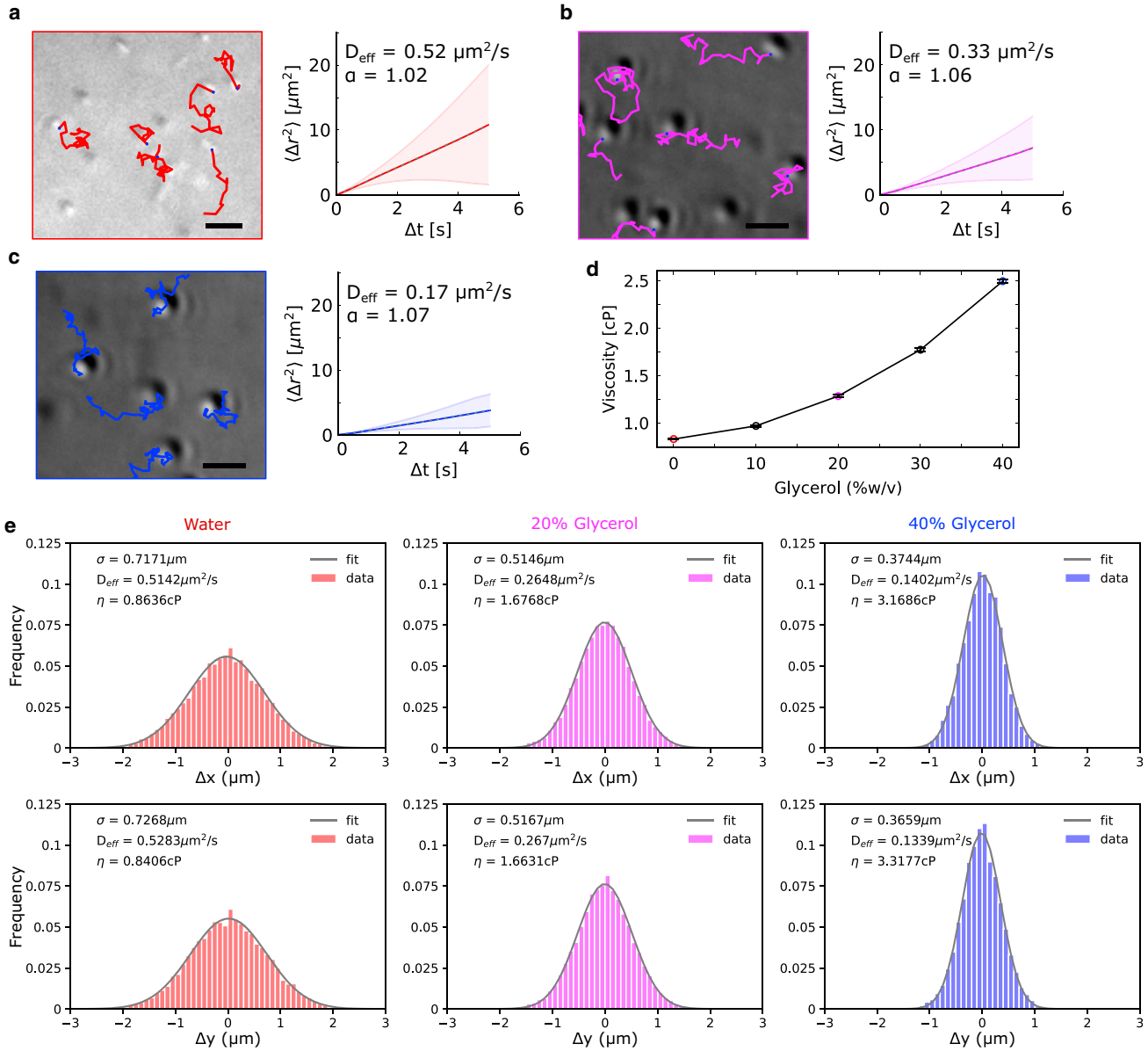

FIGURE 4 Microrheology of glycerol solutions from bead mobility. (*a–c*) 1-μm-diameter beads suspended in increasing concentrations of glycerol were imaged to measure the bead mobility. The beads were tracked (*colored lines*) and the MSD ± SD (*line with gray area* indicting SD) calculated. Track colors correspond to glycerol concentrations (%v/v) in water: (*a*) 0% (*red*), (*b*) 20% (*magenta*), and (*c*) 40% (*blue*). Scale bar, 2 μm. (*d*) Shown is the viscosity estimated from the diffusion of 1-μm-sized beads in solutions of glycerol concentrations ranging from 0 to 40%. Values represent mean ± SEM (n = 10 ROIs). (*e*) Histograms of the instantaneous displacement of beads in X and Y obtained from tracking were fitted to a standard Gaussian. The effective diffusion coefficient D was then estimated based on $\sigma = \sqrt{2Dt}$ from the Gaussian fit and the Stokes-Einstein relation used to estimate viscosity η. To see this figure in color, go online.

analysis of average trajectories along both axes is 40 mHz (Fig. 3 *c*). Our estimate is based on the statistics of $\sim 10^2$ trajectories of yolk granules per cell. This estimate matches the reported oscillatory frequency of 40 mHz measured using pairs of centrosomes in each cell (25,26,32). Thus, our approach to yolk-granule tracking provides detailed spatiotemporal information and better statistics as compared with centrosome movement to understand the mechanics of cytoplasmic flows.

Microrheology of beads in glycerol solutions

We test the accuracy of our approach to object tracking by quantifying the diffusive mobility of 1-μm polystyrene beads in multiple dilutions of glycerol solutions (0–40% v/v) from DIC image time series (Videos S2, S3, and S4). From the trajectories of the bead mobility, we estimated the MSD ($\langle r^2 \rangle$) as a function of time t of multiple beads and fit it to a model of diffusive mobility $\langle r^2 \rangle = 4Dt^{\alpha}$ (Fig. 4, *a–c*) as described in our previous work (34). The value of the anomalous diffusion exponent α obtained from fitting is $\sim$1, confirming that bead mobility is diffusive. The diffusion coefficient D is then used to estimate the viscosity η (Fig. 4 *d*) based on the Stokes-Einstein relation $\eta = k_B T/D6\pi r$, where r is the granule radius and $k_B T$ the thermal energy scale. We also estimated the value of viscosity from the same trajectories by alternatively following a method originally described by Perrin (36) by fitting Gaussian functions to the one-dimensional displacement along x and y axes (Fig. 4 *e*). Both methods yield viscosity values that are consistent with published values (40) for glycerol solutions (Fig. S10). Thus, we believe our method can serve as a convenient tool for microrheology and mobility of label-free DIC imaging of micron-sized objects, both intracellular and in vitro.

CONCLUSIONS

The yolk-granule mobility in *C. elegans* embryos demonstrated here suggests the frequency of oscillation of granules matches that of the spindle movement. Although it once more suggests the passive nature of yolk-granule mobility, it also provides a spatiotemporal readout of the forces that drive spindle motility. The previous estimates of the viscous drag acting on the spindles (22,41) and more recent measurements of the viscoelastic nature of the cytoplasm (42) suggest the relevance of such a tool for quantifying cytoplasmic flows. Combining the measurement of intracellular yolk-granule mobility with spindle movement could improve our understanding of the mechanobiology of asymmetric cell division. Indeed, the proliferation of deep-learning methods in cell image analysis, as exemplified by the effective use of U-nets for segmentation from bright-field images (43), suggests the approaches we describe in combination with learning approaches could further improve detection and analysis. Our implementation of the tool as a GUI with interactive parameter optimization as well as choice of multiple filters is likely to allow for use on multiple data sets. In conclusion, our approach represents a general method for segmentation and tracking of both in vitro and in vivo DIC microscopy data. In the future, this tool could improve our understanding of subcellular mechanics using label-free microscopy for cellular and developmental processes, not just limited to the *C. elegans* embryo.

SUPPORTING MATERIAL

Supporting Material can be found online at https://doi.org/10.1016/j.bpj.2020.12.013.

AUTHOR CONTRIBUTIONS

Y.K.J., R.C., and D.K. wrote the software. Y.K.J., D.K., and R.C. analyzed and validated it. Y.K.J. and C.A.A. performed the experiments. C.A.A. wrote the manuscript, supervised the project, and acquired the funding.

ACKNOWLEDGMENTS

We are grateful to Marie Delattre for valuable discussions about the nematode embryo data. Niruj Mohan Ramanujam provided useful critical feedback about the filter description.

This work is supported by a BigData grant BT/PR16591/BID/7/673/2016 from the Department of Biotechnology, Government of India to C.A.A. Y.K.J. was supported by a fellowship from DST-INSPIRE and the Department of Biotechnology, Government of India (BT/PR16591/BID/7/673/2016). R.C. was supported by the University Grants Commission (UGC F.2–14/2011 (SA-1)), Government of India, and a postdoctoral fellowship from IISER Pune and CEFIPRA Grant 62T5-D. D.K. is supported by a fellowship from the Department of Biotechnology (DBT/JRF/BET-18/I/2018/AL/188) and CNRS-IISER Pune joint PhD program.

REFERENCES

1. Allen, R. D., G. B. David, and G. Nomarski. 1969. The zeiss-Nomarski differential interference equipment for transmitted-light microscopy. *Z. Wiss. Mikrosk. Mikrosk. Tech.* 69:193–221.
2. Zernike, F. 1942. Phase contrast, a new method for the microscopic observation of transparent objects. *Physica.* 9:686–698.
3. Dixit, R., and R. Cyr. 2003. Cell damage and reactive oxygen species production induced by fluorescence microscopy: effect on mitosis and guidelines for non-invasive fluorescence microscopy. *Plant J.* 36:280–290.
4. Guberman, J. M., A. Fay, …, Z. Gitai. 2008. PSICIC: noise and asymmetry in bacterial division revealed by computational image analysis at sub-pixel resolution. *PLoS Comput. Biol.* 4:e1000233.
5. Rogers, S. S., T. A. Waigh, …, J. R. Lu. 2007. Precise particle tracking against a complicated background: polynomial fitting with Gaussian weight. *Phys. Biol.* 4:220–227.
6. Sliusarenko, O., J. Heinritz, …, C. Jacobs-Wagner. 2011. High-throughput, subpixel precision analysis of bacterial morphogenesis and intracellular spatio-temporal dynamics. *Mol. Microbiol.* 80:612–627.

7. Zeisel, A., A. Yitzhaky, …, E. Domany. 2013. qCMA: a desktop application for quantitative collective cell migration analysis. *J. Biomol. Screen.* 18:356–360.
8. Piccinini, F., A. Kiss, and P. Horvath. 2016. CellTracker (not only) for dummies. *Bioinformatics.* 32:955–957.
9. Athale, C. A., and H. Chaudhari. 2011. Population length variability and nucleoid numbers in *Escherichia coli*. *Bioinformatics.* 27:2944–2948.
10. Chalfoun, J., M. Majurski, …, M. Brady. 2015. Empirical gradient threshold technique for automated segmentation across image modalities and cell lines. *J. Microsc.* 260:86–99.
11. King, S. V., A. Libertun, …, C. Preza. 2008. Quantitative phase microscopy through differential interference imaging. *J. Biomed. Opt.* 13:024020.
12. Obara, B., M. A. J. Roberts, …, V. Grau. 2013. Bacterial cell identification in differential interference contrast microscopy images. *BMC Bioinformatics.* 14:134.
13. Crocker, J. C., and B. D. Hoffman. 2007. Multiple-particle tracking and two-point microrheology in cells. *Methods Cell Biol.* 83:141–178.
14. Danuser, G., P. T. Tran, and E. D. Salmon. 2000. Tracking differential interference contrast diffraction line images with nanometre sensitivity. *J. Microsc.* 198:34–53.
15. Fanti, Z., M. E. Martinez-Perez, and F. F. De-Miguel. 2011. NeuronGrowth, a software for automatic quantification of neurite and filopodial dynamics from time-lapse sequences of digital images. *Dev. Neurobiol.* 71:870–881.
16. Bormuth, V., J. Howard, and E. Schäffer. 2007. LED illumination for video-enhanced DIC imaging of single microtubules. *J. Microsc.* 226:1–5.
17. Brangwynne, C. P., C. R. Eckmann, …, A. A. Hyman. 2009. Germline P granules are liquid droplets that localize by controlled dissolution/condensation. *Science.* 324:1729–1732.
18. Vig, D. K., A. E. Hamby, and C. W. Wolgemuth. 2016. On the quantification of cellular velocity fields. *Biophys. J.* 110:1469–1475.
19. Cerbino, R., and V. Trappe. 2008. Differential dynamic microscopy: probing wave vector dependent dynamics with a microscope. *Phys. Rev. Lett.* 100:188102.
20. Feriani, L., M. Juenet, …, P. Cicuta. 2017. Assessing the collective dynamics of motile cilia in cultures of human airway cells by multiscale DDM. *Biophys. J.* 113:109–119.
21. Gönczy, P., H. Schnabel, …, R. Schnabel. 1999. Dissection of cell division processes in the one cell stage *Caenorhabditis elegans* embryo by mutational analysis. *J. Cell Biol.* 144:927–946.
22. Grill, S. W., P. Gönczy, …, A. A. Hyman. 2001. Polarity controls forces governing asymmetric spindle positioning in the *Caenorhabditis elegans* embryo. *Nature.* 409:630–633.
23. Blanchoud, S., Y. Budirahardja, …, P. Gönczy. 2010. ASSET: a robust algorithm for the automated segmentation and standardization of early *Caenorhabditis elegans* embryos. *Dev. Dyn.* 239:3285–3296.
24. Giurumescu, C. A., and A. D. Chisholm. 2011. Cell identification and cell lineage analysis. *Methods Cell Biol.* 106:325–341.
25. Farhadifar, R., and D. Needleman. 2014. Automated segmentation of the first mitotic spindle in differential interference contrast microcopy images of *C. elegans* embryos. *Methods Mol. Biol.* 1136:41–45.
26. Cluet, D., P. N. Stébé, …, M. Delattre. 2014. Automated high-throughput quantification of mitotic spindle positioning from DIC movies of Caenorhabditis embryos. *PLoS One.* 9:e93718.
27. Gönczy, P., S. Grill, …, A. A. Hyman. 2001. Spindle positioning during the asymmetric first cell division of *Caenorhabditis elegans* embryos. *Novartis Found. Symp.* 237:164–175, discussion 176–181.
28. Grill, S. W., J. Howard, …, A. A. Hyman. 2003. The distribution of active force generators controls mitotic spindle position. *Science.* 301:518–521.
29. Grill, S. W., K. Kruse, and F. Jülicher. 2005. Theory of mitotic spindle oscillations. *Phys. Rev. Lett.* 94:108104.
30. Pecreaux, J., J. C. Röper, …, J. Howard. 2006. Spindle oscillations during asymmetric cell division require a threshold number of active cortical force generators. *Curr. Biol.* 16:2111–2122.
31. Kozlowski, C., M. Srayko, and F. Nedelec. 2007. Cortical microtubule contacts position the spindle in *C. elegans* embryos. *Cell.* 129:499–510.
32. Valfort, A.-C., C. Launay, …, M. Delattre. 2018. Evolution of mitotic spindle behavior during the first asymmetric embryonic division of nematodes. *PLoS Biol.* 16:e2005099.
33. Khetan, N., and C. A. Athale. 2016. A motor-gradient and clustering model of the centripetal motility of MTOCs in meiosis I of mouse oocytes. *PLoS Comput. Biol.* 12:e1005102.
34. Athale, C. A., A. Dinarina, …, E. Karsenti. 2014. Collective behavior of minus-ended motors in mitotic microtubule asters gliding toward DNA. *Phys. Biol.* 11:016008.
35. Jones, E., T. Oliphant, …, P. Peterson. 2001. SciPy: Open source scientific tools for Python http://www.scipy.org/.
36. Perrin, J. 1909. Mouvement brownien et réalité moléculaire (Brownian movement and molecular reality). *Ann. Chim. Phys.* 8:5–114.
37. Assirati, L., N. Silva, …, O. Bruno. 2014. Performing edge detection by difference of Gaussians using q-Gaussian kernels. *J. Phys. Conf. Ser.* 490:012020.
38. Otsu, N. N. 1979. A threshold selection method from gray-level histograms. *IEEE Trans. Syst. Man Cybern.* 9:62–66.
39. Shinar, T., M. Mana, …, M. J. Shelley. 2011. A model of cytoplasmically driven microtubule-based motion in the single-celled *Caenorhabditis elegans* embryo. *Proc. Natl. Acad. Sci. USA.* 108:10508–10513.
40. Segur, J. B., and H. E. Oberstar. 1951. Viscosity of glycerol and its aqueous solutions. *Ind. Eng. Chem.* 43:2117–2120.
41. Grill, S. W. 2002. The mechanics of asymmetric spindle positioning in the Caenorhabditis elegans embryo. PhD thesis (Physik-Department, Techniche Universitaet Muenchen).
42. Garzon-Coral, C., H. A. Fantana, and J. Howard. 2016. A force-generating machinery maintains the spindle at the cell center during mitosis. *Science.* 352:1124–1127.
43. Falk, T., D. Mai, …, O. Ronneberger. 2019. U-Net: deep learning for cell counting, detection, and morphometry. *Nat. Methods.* 16:67–70.

Biophysical Journal, Volume *120*

Supplemental Information

Quantifying Intracellular Particle Flows by DIC Object Tracking

Anushree R. Chaphalkar, Yash K. Jawale, Dhruv Khatri, and Chaitanya A. Athale

SUPPORTING MATERIAL

Quantifying Intracellular Particle Flows by DIC Object Tracking (DICOT)

Anushree R. Chaphalkar, Yash K. Jawale, Dhruv Khatri and Chaitanya A. Athale*

Contents

1 Algorithm

The algorithm is described in Box **??**.

Algorithm 1 The routine describing image filtering using SoG and segmentation.

SoG

Image, Img $\leftarrow$ INPUT(filename)
Kernel-size, $k_{size} \leftarrow$ INPUT(int)
Kernel-spread, $\sigma \leftarrow$ INPUT(float)
ObjectType, $\lambda \leftarrow$ INPUT(bright=1,dark=-1)
Sensitivity, $\phi \leftarrow$ INPUT(float)
Strength of threshold, p $\leftarrow$ INPUT(int)
$h_G''(i,j) = e^{\frac{-(x^2+y^2)}{2\sigma^2}}$
$h_G(i,j) = \frac{h_G''(i,j)}{\sum_i^{k_{size}} \sum_j^{k_{size}} h_G''}$
$h'(i,j)_G = h_G - \langle h_G \rangle$
$h_{SoG} = \lambda \cdot h_G'(i,j) - \phi \langle h_G \rangle$
imFiltered $\leftarrow h_{SoG}(i,j) \circledast Img(n_1, n_2)$
Threshold, $\tau \leftarrow$ Otsu(imFiltered)

if imFiltered(j,k)> $\sqrt[p]{\tau}$ **then**
  imFiltered(j,k)$\leftarrow$ 1
else
  imFiltered(j,k) $\leftarrow$ 0
end if

2 Supplemental Tables

Sample	k_{size}	σ	λ	ϕ	p
E. coli [DIC]	11	3.25	1	0	3
E. coli [DAPI]	11	3.25	1	0	3
Beads [Phase]	5	1.75	0	0.01	1
MT [Rh]	15	1.25	1	0	1
Rice (edge)	3	1.25	1	0	1
Rice (blob)	11	2.5	1	0	0.97

Table S1: **Parameters of the SoG filter for varied samples.** The parameters input to the SoG filter for detecting objects in diverse imaging modes (DIC, phase contrast and fluorescence microscopy) are listed, with the outputs seen in Fig. **??**.

3 Supplemental Figures

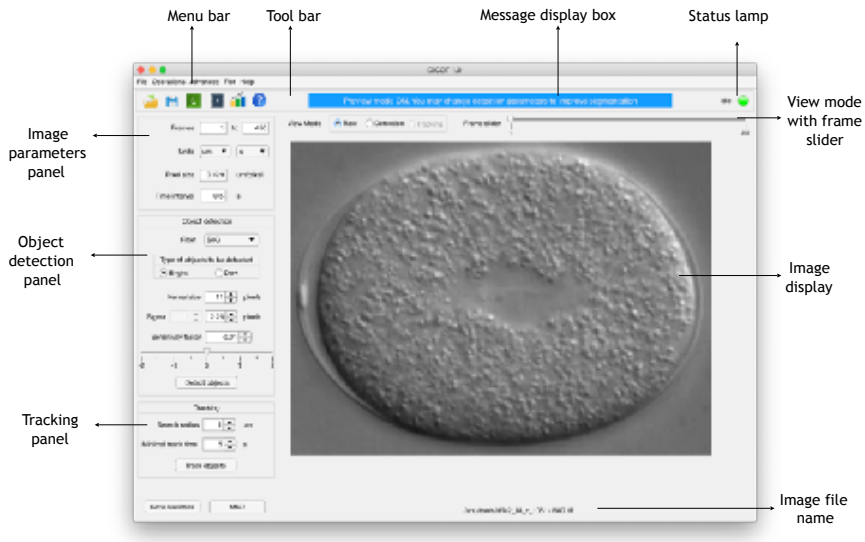

Figure S1: **GUI interface for the DIC object detection and tracking code.** The program has a GUI interface with a single pane. The menu bar can be used along with the icons to (i) select and parse the image data, (ii) detect objects and interactively view the results in the image-pane and (iii) the tracking panel to determine the criteria to track detected objects. The buttons on the very bottom export the statistics into text files as well as calculate mean square displacement (MSD) plots and fit the average curve either to an anomalous diffusion or diffusion and drift model. A detailed user guide is provided with the source code at `https://github.com/CyCelsLab/DICOT`.

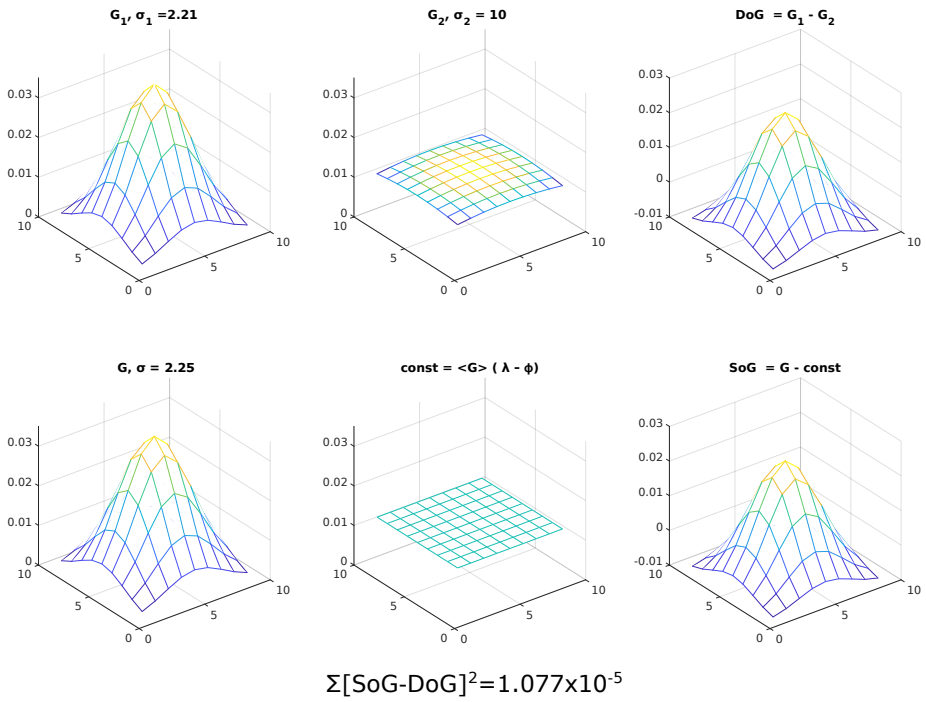

Figure S2: **The 2D profiles of comparable DoG and SoG filters.** *First row* A DoG filter is created by subtracting a Gaussian filter G_2 with $\sigma_2 = 10$ from G_1 with $\sigma_1 = 2.21$ to create a DoG filter that strongly resembles an *Second row* SoG filter. Here, the difference between a Gaussian with $\sigma = \sigma_1 = 2.5$ and a constant, the product of the mean of the Gaussian with $\lambda - \phi$ where $\lambda = 1$ is the switch parameter and $\phi = 0.01$ the sensitivity factor. The sum of square errors between these two functions is 1.07×10^{-5}.

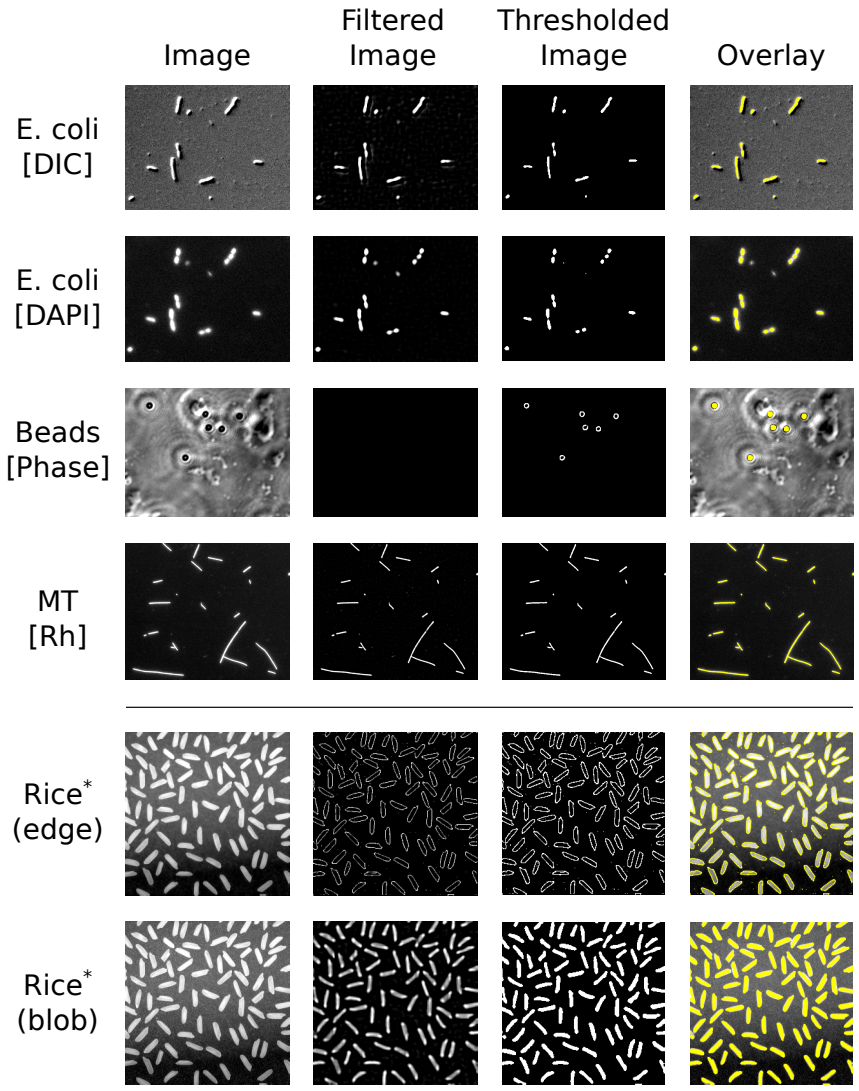

Figure S3: **SoG applied to diverse images.** Object detection from images acquired in different modes of microscopy was attempted by SoG filtering. (Top-Bottom) *Escherichia coli* cells in DIC, *E. coli* stained with DAPI in fluorescence, micron size beads in phase contrast microscopy (holes filled in threshold image before overlay), rhodamine labelled microtubules (MT) in fluorescence and rice grains (*MATLAB demo image) processed by either edge or blob-detection. DICOT parameters for each of the samples are listed in Table **??**.

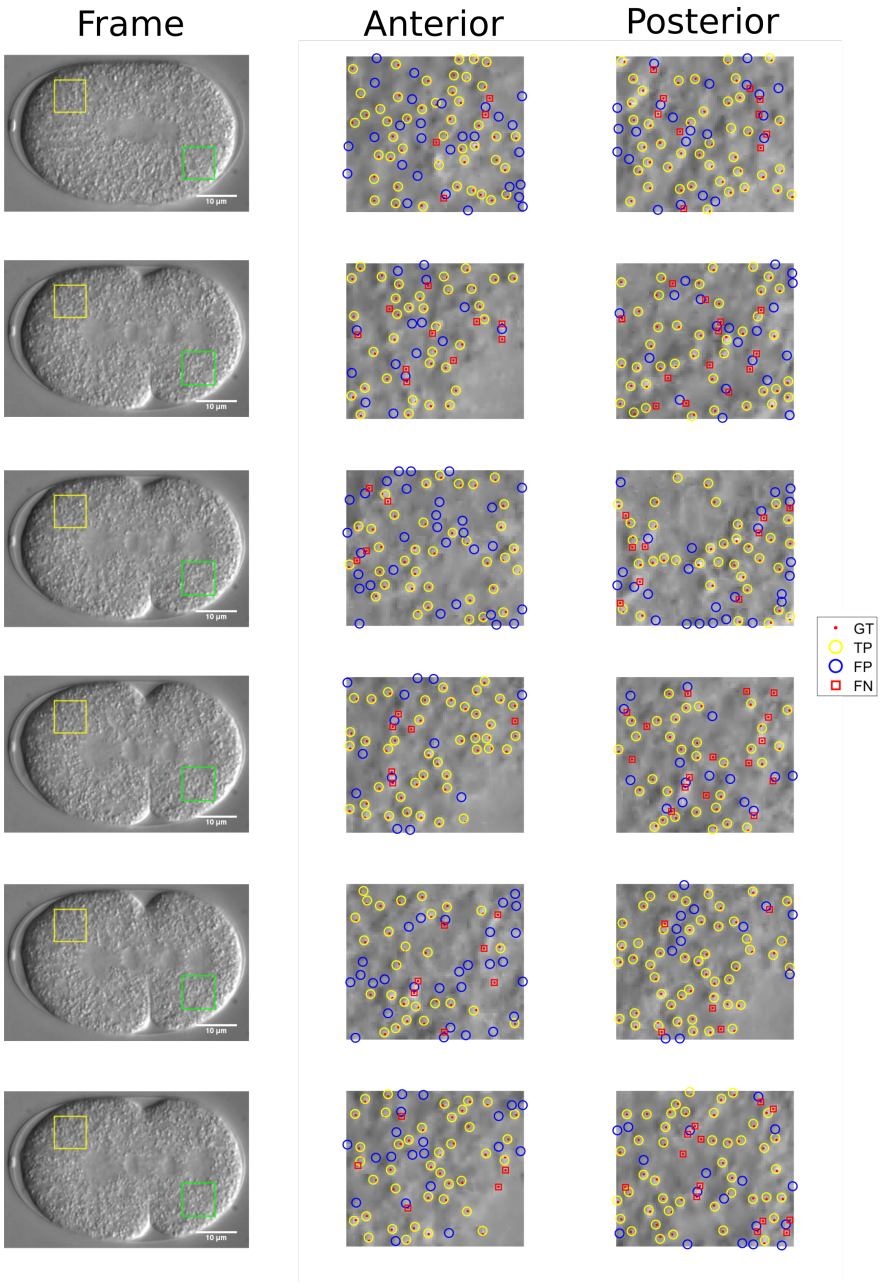

Figure S4: **Multiple ROIs used to evaluate object detection.** The *C.elegans* embryo time-series (N2_20_c_1001-1450) with frame numbers (*top to bottom*) 78, 295, 177, 335, 341, and 306 are overlaid with contour of regions of interest (ROIs) selected in anterior and posterior domains of the embryo. The representative panels from the anterior and posterior ROIs were manually annotated to mark lipid granules to serve as the ground truth GT (red dots) and after SoG image-filtering and segmentation used to determine true positives TP (blue circles), false positives FP (yellow circles) and false negatives FN (red squares), as described in the methods section. Scale bar 10 μm.

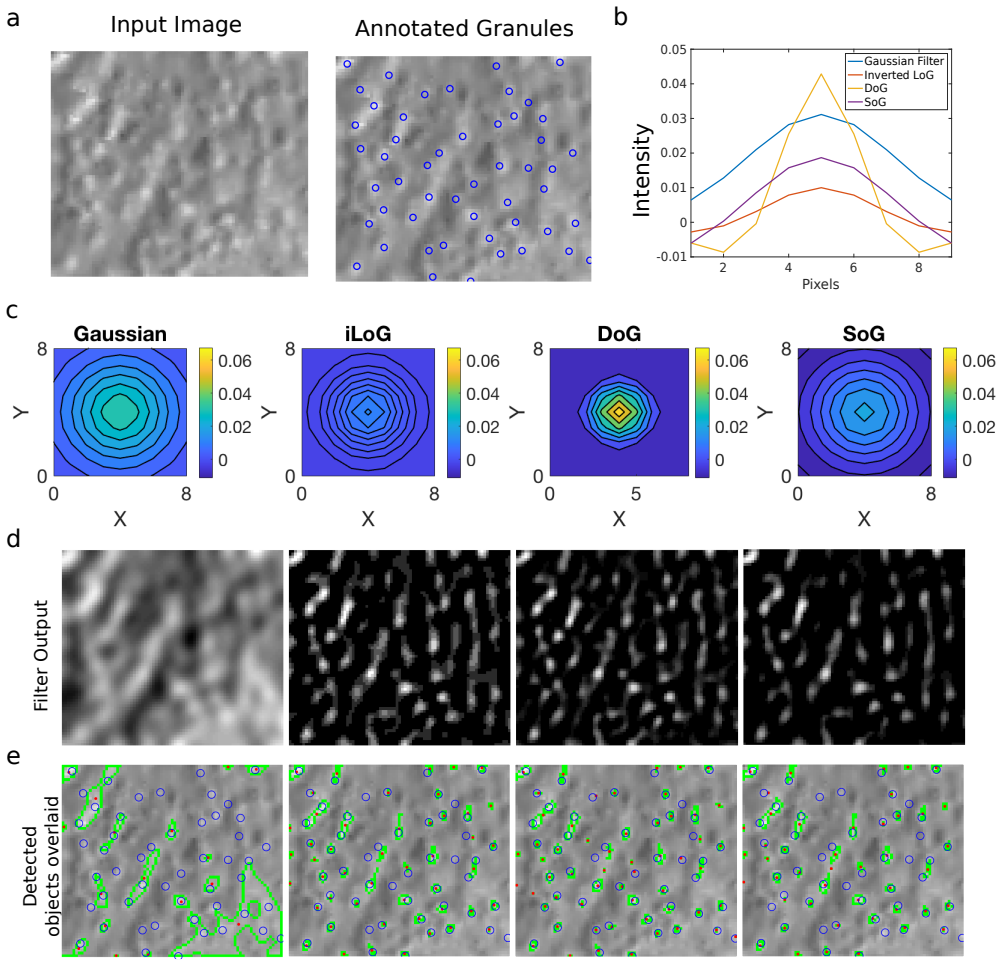

Figure S5: **Comparing filters for DIC object detection.** (a) An ROI from a mid-plane DIC image of a *C. elegans* embryo was manually annotated to mark lipid granules (blue circles). (b) Four different image filters were tested: Gaussian (blue), Inverted LoG (red), DoG (ochre) and SoG (purple). (c) Contour maps of multiple filters used to convolve the data are compared: Gaussian $\sigma = 2.25$, inverted Laplacian of Gaussian (iLoG) $\sigma = 2.25$, difference of Gaussian (DoG) taken between two functions with $\sigma = 1.25$ and 2.25 and Scaling of Gaussian (SoG) $\sigma = 2.25$. All filters have the same kernel size, i.e. 9 pixels. (c) The filtered output images (d) are then segmented by an automated threshold and the contours of detected objets (green) are used to estimate centroids (red dots) and compared to manual annotations (blue circles).

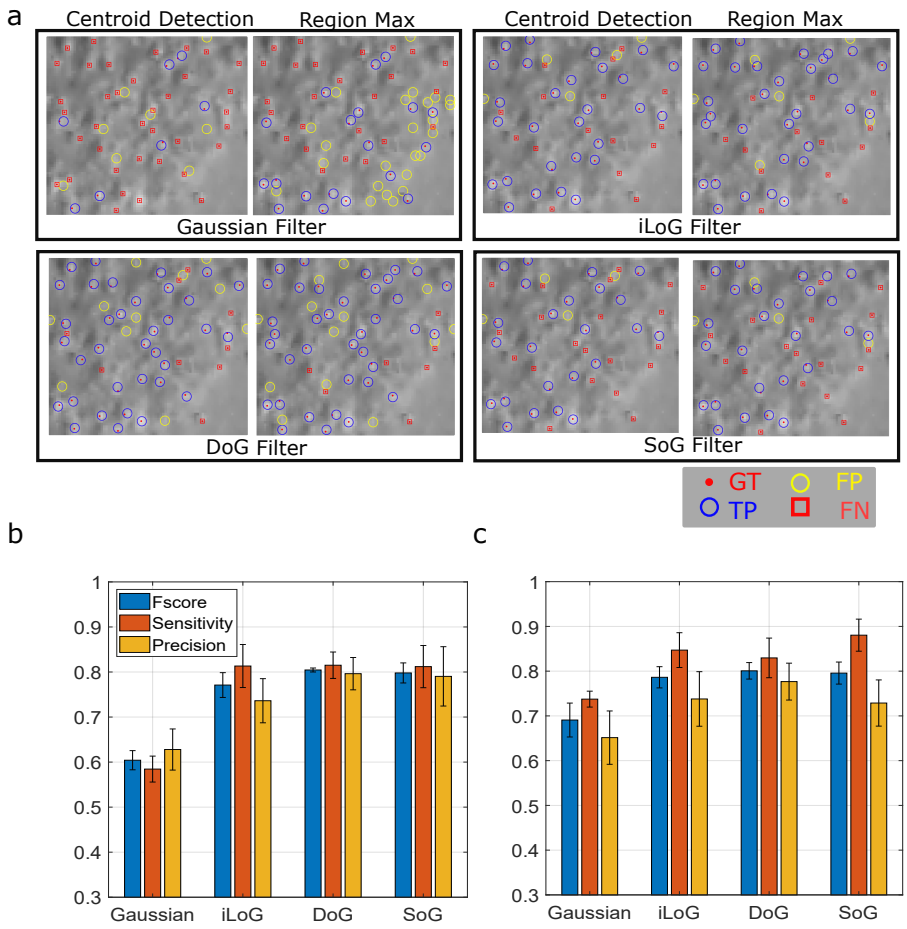

Figure S6: **Filters compared for sensitivity, precision and F1-score.** (a) An ROI from a mid-plane DIC image of a *C. elegans* embryo was manually annotated to mark lipid granules to serve as the ground truth GT (red dots) and compared to image-filtering with Gaussian, inverted Laplacian of Gaussian (iLOG), difference of Gaussian (DoG) and scaling of Gaussian (SoG). The respective true positives TP (blue circles), false positives FP (yellow circles) and false negatives FN (red squares) were determined as described in the methods section, comparing centroid and region-max based object detection. (b, c) The F-score, sensitivity and precision calculated from these comparisons for (b) centroids and (c) region-max based identification of objects are plotted.

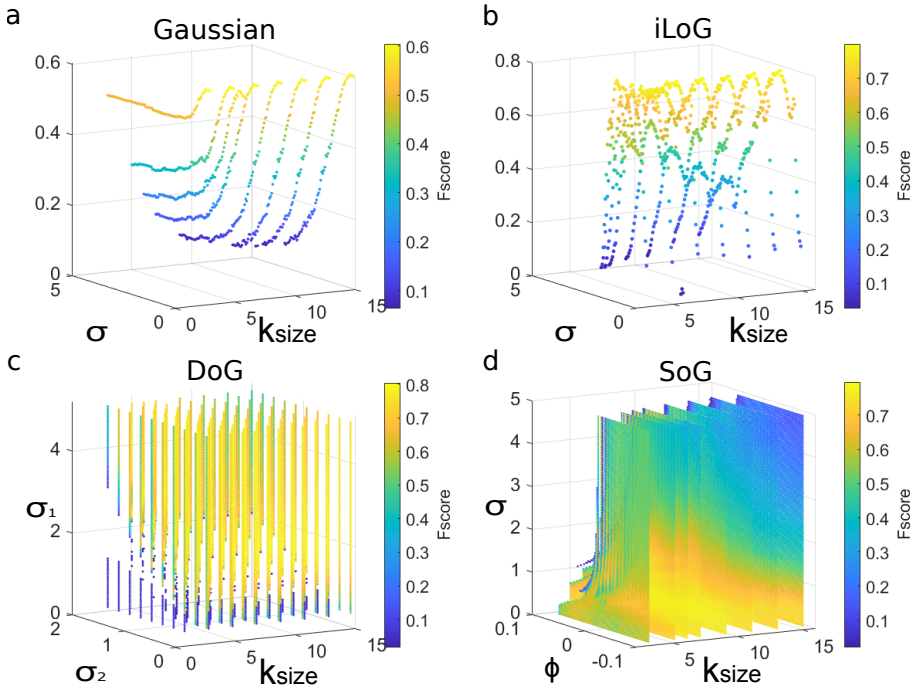

Figure S7: **Detection accuracy estimated by F1-score to compare filters.** (a) Gaussian, (b) inverted Laplacian of Gaussian (iLoG), (c) difference of Gaussian (DoG) and (d) scaling of Gaussian (SoG). For all filters the range of k_{size} was 3 to 15, σ was scanned over a range 0.1 to 5 with steps of 0.0495 while for DoG $\sigma_1 = \sigma$ while σ_2 was varied between 0.1 and 2 with steps of 0.211. For SoG the sensitivity factor ϕ was sampled between -0.1 and 0.1 with steps of 0.002. Colorbar indicates the F1-score.

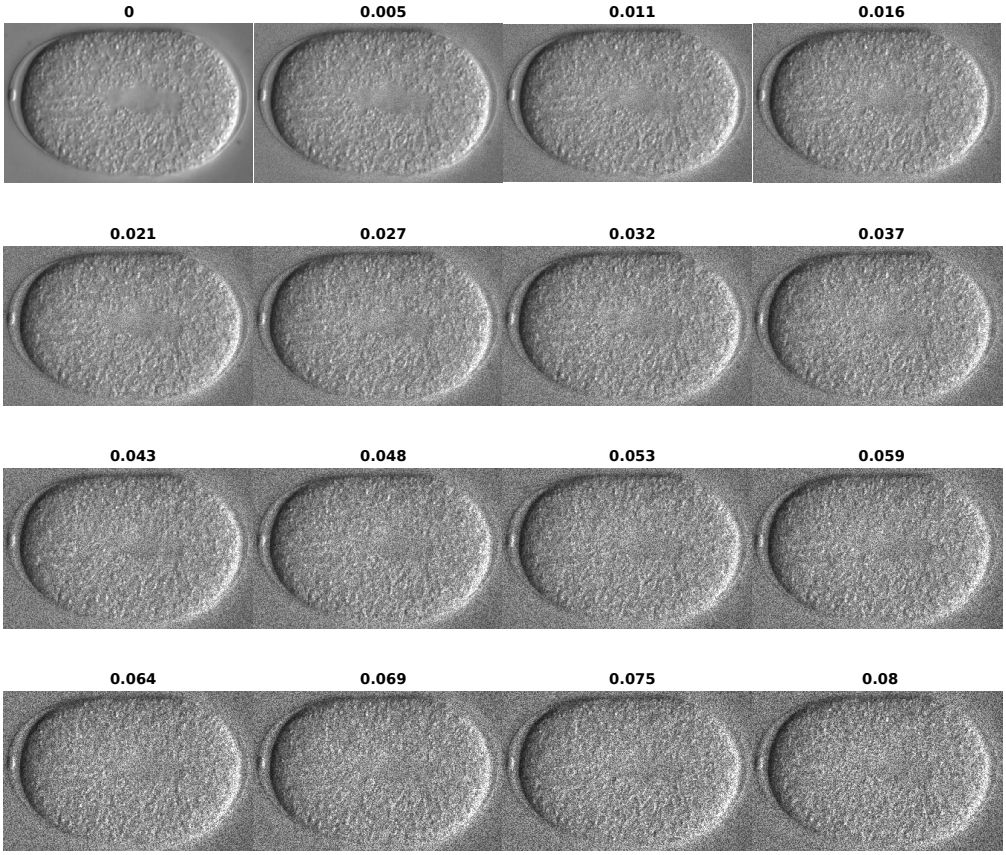

Figure S8: **Increasing noise of DIC image.** A single frame of a DIC image of *C. elegans* was subjected to increasing speckle noise with increasing variance of the noise ranging from 0 to 0.08. These images were used to test the error in positional detection using multiple filtering algorithms.

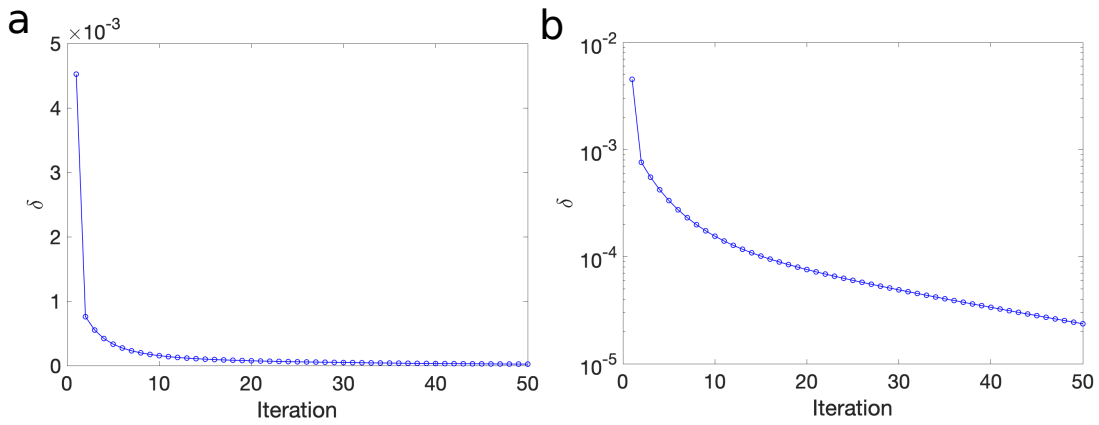

Figure S9: **Convergence of cost function to granule oscillations.** (a,b) The change of global deviation δ of the average curve to yolk granule oscillations (seen in Fig. 3(c)) are plotted on a (a) linear scale (b) semi-log scale.

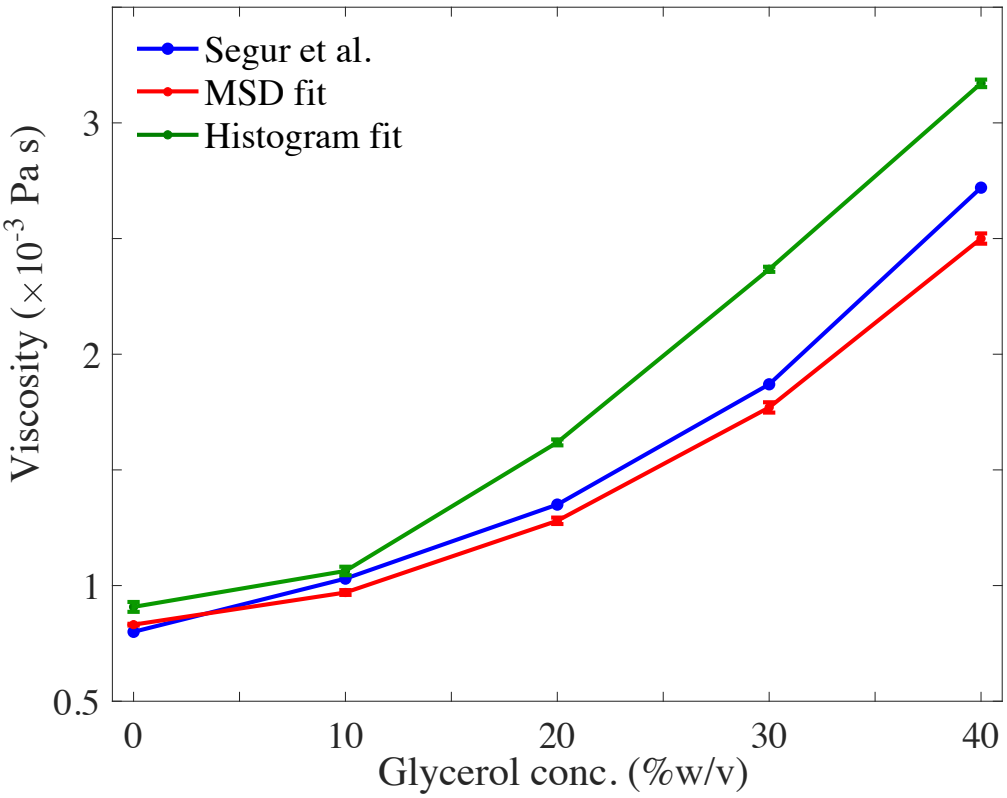

Figure S10: **Viscosity estimated using DICOT compared to literature.** The estimates of viscosity, η, obtained from tracking diffusing beads based on fitting the MSD (red) is compared to that using fits to the histogram of displacements (green). Both estimates are compared to bulk viscosity measurements of glycerol solutions [**?**]. All experimental estimates of η are mean±s.e.m. For n=10 fields of view.

4 Supplemental Videos

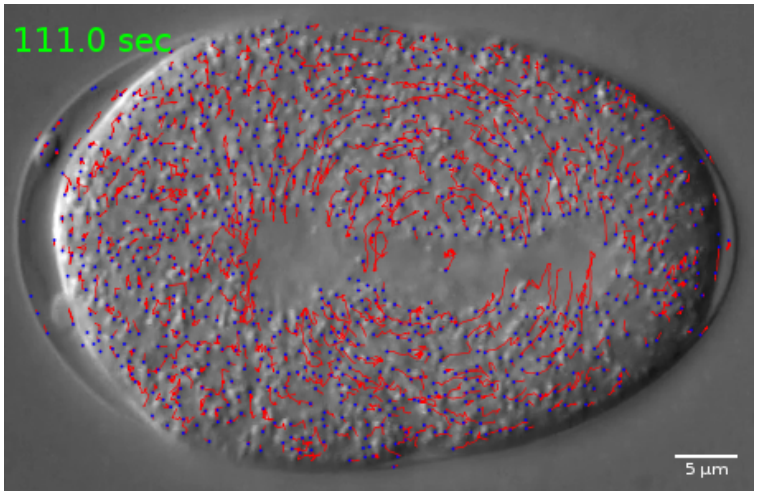

Video SV1: *C. elegans* **embryos with tracked granules.** The granules in a time series of *C.elegans* first embryonic division are tracked (blue dot - current position of granule, red line - trajectory of granules) using DIC tracking method. The time series have been described by Valfort et al. [**?**] (Image-Database). Scale: 5 μm; Δt: 0.5 s.

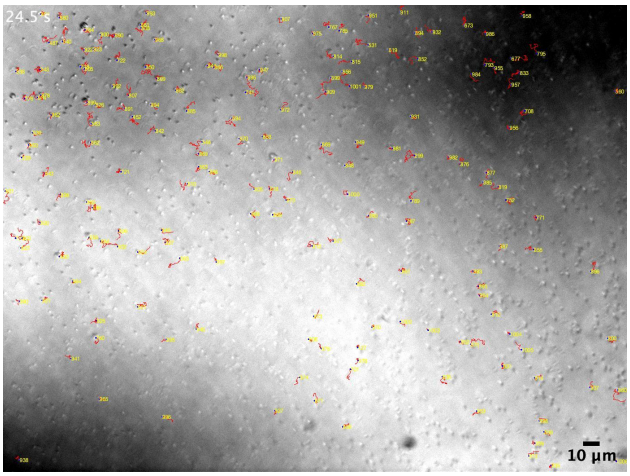

Video SV2: **Beads diffusing in water.** A representative time series of 1 μm beads diffusing in water tracked (blue dot - current position of granule, red line - trajectory of granules, yellow numbers - particle identifier) using SoG filter. Scale: 10 μm; Δt: 0.5 s

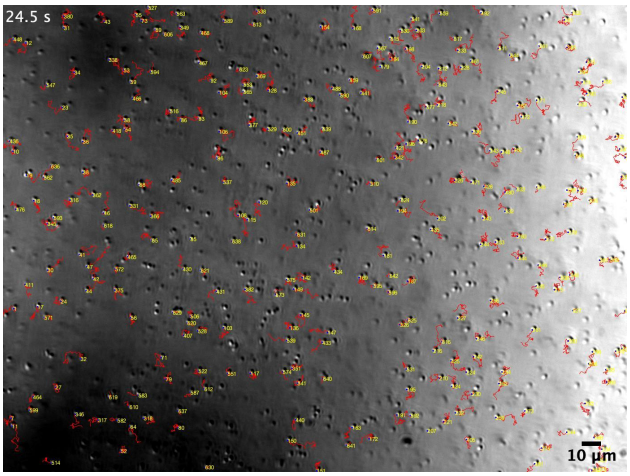

Video SV3: **Beads diffusing in 20% glycerol.** A representative time series of 1 μm beads diffusing in 20% (w/v) glycerol tracked (blue dot - current position of granule, red line - trajectory of granules, yellow numbers - particle identifier) using SoG filter. Scale: 10 μm; Δt: 0.5 s

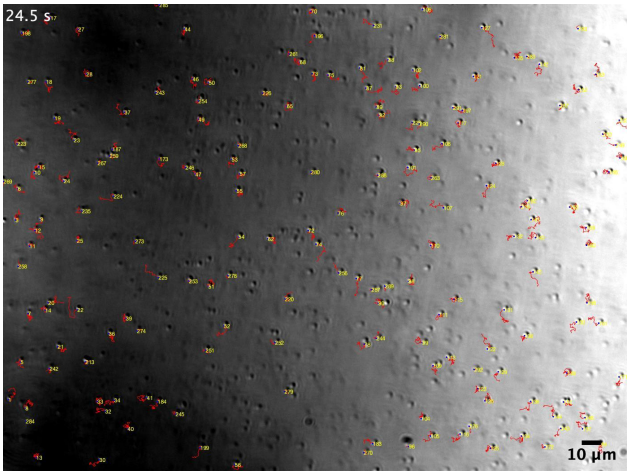

Video SV4: **Beads diffusing in 40% glycerol.** A representative time series of 1 μm beads diffusing in 40% (w/v) glycerol tracked (blue dot - current position of granule, red line - trajectory of granules, yellow numbers - particle identifier) using SoG filter. Scale: 10 μm; Δt: 0.5 s